CHEMISTRY OF MATERIALS
Cite This: Chem. Mater. 2019, 31, 4353−4363
Article
pubs.acs.org/cm

Tailoring Two-Electron-Donating Phenothiazines To Enable High-Concentration Redox Electrolytes for Use in Nonaqueous Redox Flow Batteries

N. Harsha Attanayake,[†,⊥] Jeffrey A. Kowalski,[‡,§,⊥] Katharine V. Greco,[‡,§] Matthew D. Casselman,[†] Jarrod D. Milshtein,[‡,∥] Steven J. Chapman,[†] Sean R. Parkin,[†] Fikile R. Brushett,*[,‡,§] and Susan A. Odom*[,†]

[†]Department of Chemistry, University of Kentucky, Lexington, Kentucky 40506, United States
[‡]Joint Center for Energy Storage Research, Massachusetts Institute of Technology, Cambridge, Massachusetts 02139, United States
[§]Department of Chemical Engineering and [∥]Department of Materials Science and Engineering, Massachusetts Institute of Technology, Cambridge, Massachusetts 02139, United States

Supporting Information

ABSTRACT: This study aims to advance our understanding of the physical and electrochemical behavior of nonaqueous redox electrolytes at elevated concentrations and to develop experimentally informed structure−property relationships that may ultimately enable deterministic design of soluble multielectron-transfer organic redox couples for use in redox flow batteries. To this end, we functionalized a phenothiazine core to simultaneously impart two desired properties: high solubility and multiple electron transfer. Specifically, we report the synthesis, solubility, and electrochemical analysis of two new phenothiazine derivatives, 3,7-dimethoxy-*N*-(2-(2-methoxyethoxy)ethyl)phenothiazine and *N*-ethyl-3,7-bis(2-(2-methoxyethoxy)ethoxy)phenothiazine, both of which are two-electron donors that are miscible with nonaqueous electrolytes. This dual-property improvement compared to previous phenothiazine derivatives allows for extended symmetric flow cell experiments for 460 h of cycling of a multielectron transfer system at high concentrations (0.3 M active material, 0.6 M faradaic concentration), better representing practical devices.

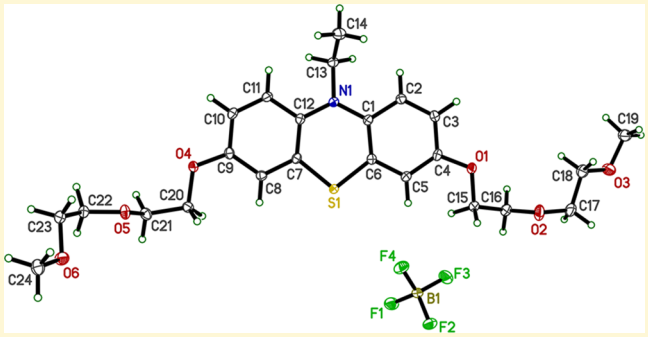

INTRODUCTION

Stationary energy storage systems facilitate the integration of intermittent, renewable energy sources (e.g., wind and solar), improve the efficiency of the existing fossil fuel infrastructure, and provide resiliency in case of emergency.[1,2] Although many storage technologies are under consideration for grid applications, redox flow batteries (RFBs) have shown particular promise for long duration needs.[3−7] In an RFB, energy is stored in electrochemically active materials that are dissolved or suspended in electrolyte solutions held in separate reservoirs. To charge or discharge the battery, the liquid electrolytes are pumped through a power-converting reactor, where they are oxidized or reduced to store or release energy before being returned to their respective reservoirs.[4,8−11] Batteries of this architecture are well suited for grid storage because of their decoupled energy (external reservoir size) and power (reactor size) ratings, relatively simple manufacturing, long service life, and location independence.[12−14] Despite these promising features, the widespread adoption of RFBs is limited by their high costs relative to competing technologies, motivating the exploration of new redox chemistries that could enable low-cost storage solutions.[15,16]

State-of-the-art RFBs are based on acidic aqueous electrolyte solutions containing molar concentrations of redox-active transition-metal salts based on vanadium, iron, or chromium.[6,12,17−23] However, there is a growing body of work around redox couples based on organic materials, including small molecules,[3−5,9,24−35] metal-centered coordination complexes,[21−23,36−42] and macromolecules,[43−45] such as polymers[45−47] and colloids.[5,48] Organic molecules are of particular interest because they are primarily composed of earth-abundant atoms (e.g., carbon, oxygen, and hydrogen), which, in turn, may lower active material costs. Further, physical and electrochemical properties can be tailored through molecular functionalization to improve performance (e.g., increasing solubility and chemical stability), enabling purpose-built redox couples.[3,4,28,49−51] The exploration of organic redox couples

Received: November 15, 2018
Revised: May 5, 2019
Published: May 7, 2019

DOI: 10.1021/acs.chemmater.8b04770
Chem. Mater. 2019, 31, 4353−4363

has also motivated the evaluation of nonaqueous electrolytes that enable the use of materials that are incompatible with aqueous electrolytes. Although these developments offer exciting new pathways toward low-cost energy storage systems,[15] designing materials capable of meeting economic targets typically requires multiproperty optimization of a molecular core, presenting significant synthetic challenges. For example, although a wide range of organic redox couples show promising activity at low concentrations,[25,28,38,39,52,53] for application in RFBs, materials must be soluble and stable in all states of charge at high (molar) concentrations. Moreover, electrochemical testing of materials at high concentrations and over extended time periods typically requires an engineered experimental apparatus and analytical techniques that extend beyond canonical electrochemical methods. Additionally, enabling such testing requires multigram batches of high-purity materials which, in turn, necessitate synthesis procedures with a minimal number of high yield steps. Consequently, only a few redox couples, typically based on well-established molecular families (e.g., anthraquinones,[28,54] nitroxyl radicals,[9,55,56] dialkoxybenzenes,[52,57] and phenothiazines[4,14,28,39]), have been demonstrated under conditions approaching those envisioned for practical embodiments.

Advancing the science and engineering of organics for use in RFBs requires improvements in our understanding of the physical and electrochemical behavior of nonaqueous electrolytes containing elevated concentrations of organic redox couples. In this study, our specific focus is the performance and longevity of highly soluble, multielectron redox couples. As illustrated in Figure 1, we seek to combine previous

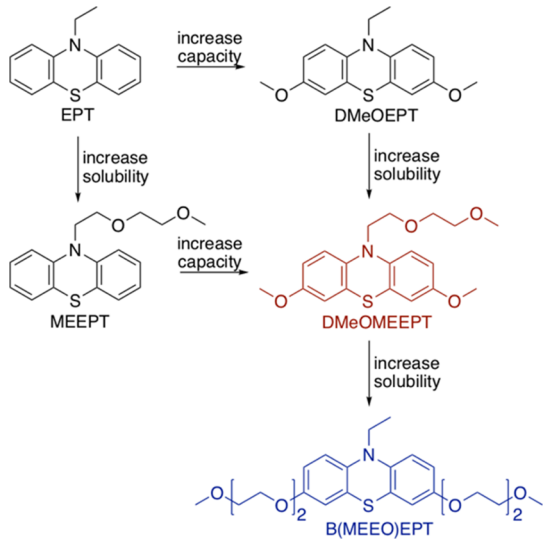

Figure 1. Representations of the chemical structures of EPT, MEEPT, DMeOEPT, DMeOMEEPT (red), and B(MEEO)EPT (blue). The molecules are vertically arranged to show an increase in the relative solubility from top to bottom and are horizontally arranged to show an increase in dication stability from left to right.

independent efforts to impart greater molecular solubility with an overarching goal of increasing the volumetric charge-storage capacity of the resultant electrolytes. Initially, we showed improvement of *N*-ethylphenothiazine (EPT, Figure 1) by increasing its solubility through the incorporation of an oligoglycol chain at the *N* position, leading to *N*-(2-(2-methoxyethoxy)-ethyl)phenothiazine (MEEPT, Figure 1).[4] This functionalization increased solubility across all states of charge such that the neutral species was a liquid that is miscible in polar aprotic solvents common to battery electrolytes, and further, the solubility of the charged species increased fivefold as compared to that of the parent compound. More recently, in an attempt to increase the intrinsic capacity of the parent EPT, we reported that introducing methoxy groups positioned para to nitrogen (3 and 7 positions) resulted in a marked improvement in stability of the dication of *N*-ethyl-3,7-dimethoxyphenothiazine (DMeOEPT, Figure 1).[39] DMeOEPT was insufficiently soluble (<0.1 M in all states of charge) to enable meaningful flow cell experiments, highlighting the need for further modification of this two-electron-donating core to achieve the high concentrations necessary for the flow cell analysis.

Here, we report the synthesis, solubility, and electrochemical analysis of two new phenothiazine derivatives that simultaneously enhance solubility and support multiple electron transfers. The first, 3,7-dimethoxy-*N*-(2-(2-methoxyethoxy)-ethyl)phenothiazine (DMeOMEEPT, Figure 1, red), combines the results from our previous work by installing an oligoglycol chain at the *N* position of the DMeOEPT structure. The second extends the methoxy groups at the 3 and 7 positions with oligoglycol chains, yielding *N*-ethyl-3,7-bis(2-(2-methoxyethoxy)ethoxy)phenothiazine (B(MEEO)EPT, Figure 1, blue). Compared to two-electron-donating DMeOEPT, both derivatives exhibit greater solubility. This dual-property improvement allows for the evaluation of a multielectron transfer system at high concentrations via symmetric flow cell cycling experiments and begins to lay the foundation for studying multiproperty structure−function relationships under conditions relevant to RFBs.

EXPERIMENTAL SECTION

Materials. Phenothiazine (≥99%), sodium hydride (60% dispersion in mineral oil), and copper(I) iodide (≥98%) were purchased from Acros Organics. Diethylene glycol monomethyl ether (99%) and methyl formate (98%) were purchased from Tokyo Chemical Incorporated. Nitrosonium tetrafluoroborate (98%) was purchased from Alfa Aesar and was stored and weighed in an argon-filled glovebox (MBraun, O_2 < 0.1 ppm, H_2O < 0.5 ppm). Anhydrous pyridine (99.8%), *N*-bromosuccinimide (99%), anhydrous methanol (99.8%), and sodium (99.9%) were purchased from Sigma-Aldrich. Other solvents were purchased from VWR. The silica gel (65 × 250 mesh) was purchased from Sorbent Technologies. ^{1}H and ^{13}C NMR spectra were obtained on 400 MHz Varian spectrometers in DMSO-d_6 from Cambridge Isotope Laboratories. Mass spectra were obtained on an Agilent 5973 Network mass selective detector attached to the Agilent 6890N Network GC system. Elemental analyses were performed by Atlantic Microlab, Inc. Solubility tests and cyclic voltammetry measurements were performed in an argon-filled glovebox (MBraun LabMaster, O_2 < 0.1 ppm, H_2O < 5 ppm).

EPT,[1] MEEPT,[2] *N*-ethyl-3,7-dibromophenothiazine (DBrEPT),[3] DMeOEPT, and *N*-ethyl-3,7-dimethoxyphenothiazine tetrafluoroborate (DMeOEPT-BF_4)[4] were synthesized as previously reported. Synthetic procedures and spectroscopic analysis for DMeOMEEPT, B(MEEO)EPT, their precursors, and radical cation salts are included in the Supporting Information, as are their representative NMR and electron paramagnetic resonance (EPR) spectra.

Solubility. The solubilities of neutral molecules, their radical cation salts, and the dication salts of DMeOEPT, DMeOMEEPT, and B(MEEO)EPT were determined in two different electrolyte solutions containing either 0.5 M tetraethylammonium tetrafluoroborate ($TEABF_4$, BASF, >99%) or 0.5 M tetraethylammonium bis-(trifluoromethane)sulfonamide (TEATFSI, IoLiTec, >99%), both dissolved in acetonitrile (ACN, BASF, 99.98%). As a result of the

DOI: 10.1021/acs.chemmater.8b04770
Chem. Mater. 2019, 31, 4353−4363

chemical oxidant used, the radical cation and dication salts contained a tetrafluoroborate anion. A known amount of active material was added to a glass vial. Then, the electrolyte solution was added slowly, and the solution was stirred between additions. Electrolyte addition was continued until the active species was completely dissolved, as determined by visual inspection. This process was performed in triplicate for each active species, and the average molar concentrations were calculated.

Cyclic Voltammetry. All cyclic voltammetry (CV) measurements were performed in an argon-filled glovebox at 26 °C (ambient glovebox temperature) using a VSP-300 potentiostat (Bio-Logic). CV measurements were performed in 0.5 M TEATFSI/ACN with either a 3 mm diameter glassy carbon macroelectrode (CH Instruments, Inc.) or an 11 μm diameter carbon fiber microelectrode (CH Instruments, Inc.). Before each measurement, both working electrodes were polished on a MicroCloth pad containing an aqueous slurry of 0.05 μm alumina powder (Buehler Ltd.), rinsed with deionized water (Millipore), and wiped with lens paper. For all experiments, the counter electrode was a gold coil (CH Instruments, Inc.), and a fritted Ag/Ag^+ electrode (fill solution: 0.1 M $AgBF_4$ [Alfa Aesar, 99%], 0.5 M TEATFSI, propylene carbonate [BASF, 99.98%]) was used as the pseudo reference electrode. To reference the measured redox potentials to the ferrocenium/ferrocene ($Cp_2Fe^{+/0}$) redox couple, before each measurement, an additional CV was taken in the electrolyte containing 5 mM ferrocene (Sigma-Aldrich, 98%).

The macroelectrode was used to determine the redox potential (average of anodic and cathodic peak potentials), chemical reversibility (peak height ratio), and electrochemical reversibility (peak separation) of each redox event. Active materials were studied at 1 mM in the electrolyte, and 100% *iR* correction was applied. The cell resistance was determined using the ZIR technique (BioLogic software package), which takes impedance measurements at a frequency of 200 kHz. The resistance measured was ca. 50 Ω, which leads to a correction of less than 0.1 mV for the largest measured currents. The diffusion coefficients were analyzed using the Randles−Sevcik equation with background current corrections, according to a published procedure

$$i_p = 0.4463nFAc\left(\frac{nFD}{RT}\nu\right)^{0.5}$$

where i_p is the peak current (A), n is the number of electrons transferred (−), F is the Faraday constant (96 485 C mol^{-1}), A is the electrode area (cm^2), c is the concentration (mol cm^{-3}), D is the diffusion coefficient (cm^2 s^{-1}), R is the gas constant (8.314 J mol^{-1} K^{-1}), T is the absolute temperature (K), and ν is the scan rate (V s^{-1}).[58] Data obtained from voltammograms at scan rates of 10, 20, 30, 40, 50, 75, and 100 mV s^{-1} were used for diffusion coefficient calculations.

The microelectrode was used to probe the electrolyte solutions before and after the symmetric flow cell cycling experiments to identify the species present (neutral, radical cation, and dication). In these analyses, the dominant species in the solution is represented by the current plateau closest to zero. The magnitude of the current plateau for a microdisc electrode is given by

$$i_{ss} = 4nFrDc$$

where i_{ss} is the steady-state plateau current (A) and r is the radius of the electrode (cm).[58] For all microelectrode experiments, the scan rate was 10 mV s^{-1}.

UV−vis Spectroscopy. In an argon-filled glove box, 0.15 mM solutions of neutral, radical cation, and dication salts of DMeOMEEPT and B(MEEO)EPT were prepared in acetonitrile and pipetted into 10 mM path length optical glass cuvettes (Starna). Then, the screw-capped cuvettes were sealed and removed from the glovebox for spectral analysis. UV−vis spectra were collected in an Agilent diode-array spectrometer.

Symmetric Flow Cell Cycling. In this work, a custom-built small-volume flow cell with interdigitated flow fields was employed.[38,62] The backing plates were machined from polypropylene, which was chosen for its chemical compatibility with the materials used in this study. The flow fields were machined in-house from 3.18 mm thick impregnated graphite (product G347B, MWI Inc., Rochester, NY). The electrodes were cut to 1.7 cm × 1.5 cm dimensions from 190 ± 30 μm thick carbon paper (SGL 29 AA, SGL group, Wiesbaden, Germany) and used as received. On each side of the flow cell, two pieces of carbon paper were layered and compressed by ca. 20% during cell assembly. Daramic 175 was used as-received as the separator (Daramic LLC, Charlotte, NC). The cell was sealed using custom gaskets cut from the polytetrafluoroethylene gasket tape (Goretex Tape, Gallagher Fluid Seals Inc., King of Prussia, PA). The geometric area of the cell was 2.55 cm^2. All flow cells were assembled on the laboratory bench and then immediately transferred into an argon-filled glovebox (Innovative Technologies, O_2 < 10 ppm, H_2O < 0.1 ppm).

Perfluoroalkoxy alkane (PFA) jars (10 mL, Savillex) were used as electrolyte reservoirs, and a peristaltic pump (Masterflex L/S series) was used to recirculate the electrolyte at a constant volumetric flow rate of 10 mL min^{-1}. Norprene tubing (Masterflex) was used inside the pump head, and PFA tubing (Swagelok) connected the reservoirs to the flow cell. The Norprene tubing was attached to the PFA tubing with stainless steel compression fittings (Swagelok). The inner diameter of all tubing used was 1.6 mm.

The electrolyte used in the flow cell studies consisted of 0.3 M *N*-ethyl-3,7-bis(2-(2-methoxyethoxy)ethoxy)phenothiazine tetrafluoroborate (B(MEEO)EPT-BF_4) and 0.5 M TEATFSI in ACN. This electrolyte has a theoretical capacity of 16.1 A h L^{-1} (161 mA h), assuming two electron transfer events and 10 mL of electrolyte per side (20 mL total). Prior to cycling the symmetric flow cell, a constant current was applied to oxidize or reduce the B(MEEO)EPT-BF_4 (radical cation), such that the negative electrolyte was oxidized to *N*-ethyl-3,7-bis(2-(2-methoxyethoxy)ethoxy)phenothiazine bis(tetrafluoroborate) (B(MEEO)EPT-$(BF_4)_2$) (dication) and the positive electrolyte was reduced to B(MEEO)EPT (neutral). All cycling experiments were performed by applying a constant current density, which was determined from the geometric electrode area (2.55 cm^2). Data were collected using a VSP-300 potentiostat (Bio-Logic). Rate and stability studies were performed in the flow cell. For the rate study, which provides insight into the tradeoff between current density and accessed capacity, the current density was varied from 10 to 50 mA cm^{-2}, in increments of 10 mA cm^{-2}, for 5 cycles at each current density, and potential cutoffs of ±0.775 V were imposed. The cell was then returned to its initial current density of 10 mA cm^{-2} for 5 additional cycles. This rate study was completed in a total time of 145 h. For the stability study, which provides information about species cyclability, the flow cell underwent constant current cycling for 140 cycles (460 h) at a current density of 25 mA cm^{-2}, with potential cutoffs of ±0.775 V.

■ RESULTS AND DISCUSSION

DMeOMEEPT and B(MEEO)EPT were both prepared in three steps from commercially available materials. To synthesize DMeOMEEPT, phenothiazine was alkylated at the *N* position to append the 2-(2-methoxyethoxy)ethyl group. The alkylated product, MEEPT, was then brominated at the 3 and 7 positions after which methoxy groups were introduced, replacing the bromine atoms. By accessing two electrons per molecule, the gravimetric capacity increased from 89 to 148 mA h g^{-1} compared to MEEPT. Similarly, to synthesize B(MEEO)EPT, an alkyl group (ethyl) was first installed at the *N* position of phenothiazine to yield EPT, which was brominated at the 3 and 7 positions, and then treated with the deprotonated oligoglycol to replace the bromine atoms with 2-(2-methoxyethoxy)ethoxy groups, which leads to a gravimetric capacity of 116 mA h g^{-1}, assuming two electron transfer events. Detailed synthetic procedures, characterization,

DOI: 10.1021/acs.chemmater.8b04770
Chem. Mater. 2019, 31, 4353−4363

and the yield for each synthesis step can be found in the Supporting Information.

Materials Screening. Cyclic voltammetry was performed to analyze fundamental, short-term electrochemical behavior, including redox potentials, diffusion coefficients, and both the chemical (stability) and electrochemical (kinetic) reversibilities. Cyclic voltammograms of 1 mM EPT, MEEPT, DMeOEPT, DMeOMEEPT, and B(MEEO)EPT in 0.5 M TEATFSI/ACN are shown in Figure 2, with corresponding values for peak potentials, peak separations, and peak-current ratios reported in Table 1. On the basis of the peak separation and peak-current ratios, the first oxidation events of both new materials, DMeOMEEPT and B(MEEO)EPT, are chemically (peak-current ratio of 0.98−1.02) and electrochemically (peak separation of 60−61 mV) reversible on the CV timescale (~minutes). However, the second oxidation event is only both chemically and electrochemically reversible for B(MEEO)EPT.

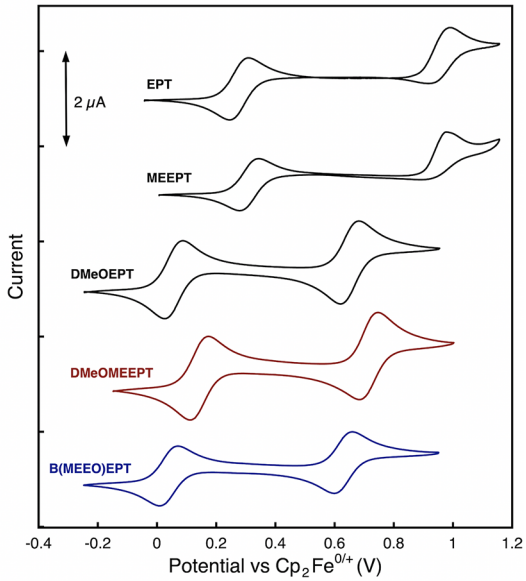

Figure 2. Cyclic voltammograms showing the first and second oxidation events of EPT, MEEPT, DMeOEPT, DMeOMEEPT, and B(MEEO)EPT at 1 mM in 0.5 M TEATFSI in ACN at a scan rate of 10 mV s^{-1}, referenced to ferrocenium/ferrocene at 0 V.

The potentials of the first and second oxidation events are similar for both DMeOMEEPT (0.093, 0.666 V vs $Cp_2Fe^{0/+}$) and B(MEEO)EPT (0.025, 0.625 V vs $Cp_2Fe^{0/+}$), with DMeOMEEPT exhibiting slightly higher (more positive) potentials than B(MEEO)EPT because of the inductive effect of the oxygen atoms in the 2-(2-methoxyethoxy)ethoxy group at the *N* position in DMeOMEEPT, which is more electron-withdrawing than the ethyl group at the equivalent (*N*) position in B(MEEO)EPT. An equivalent trend with a difference of similar magnitude is also observed for the first oxidation potentials of EPT and MEEPT, which contain the same functional groups (ethyl and 2-(2-methoxyethoxy)-ethoxy, respectively) at their *N* positions.[4] The oxidation potentials of DMeOMEEPT and B(MEEO)EPT are reduced by ca. 0.2 V compared to their *N*-alkylated equivalents MEEPT and EPT, respectively, because of the resonance contribution of the O atoms to the phenothiazine π system. A difference of similar magnitude was observed in EPT and DMeOEPT.[39] Although the first redox event is less positive than derivatives lacking alkoxy groups at the 3 and 7 positions, the average redox potential increases because of the ability to access the second redox event.

The volumetric capacity of a flow cell is limited by the solubility of the least soluble species. To determine this upper bound, the solubility of each relevant state of charge (neutral, radical cation, and dication) was measured. To perform this measurement, radical cation and dication salts of DMeO-MEEPT and B(MEEO)EPT were prepared and isolated as solids via chemical oxidation. Chemical oxidation with one or two equivalents of $NOBF_4$ results in electron transfer from the phenothiazine core to the nitrosonium (NO^+) cation, forming one or two equivalents of the neutral NO gas and either the tetrafluoroborate salt of the radical cation or the bis-(tetrafluoroborate) salt of the dication, respectively. UV−vis spectra of the oxidized species verify that unique products form, as evidenced by features distinctive both from each other and from the neutral starting material, as shown for B(MEEO)EPT in Figure 3 (see Figure S8 for the UV−vis

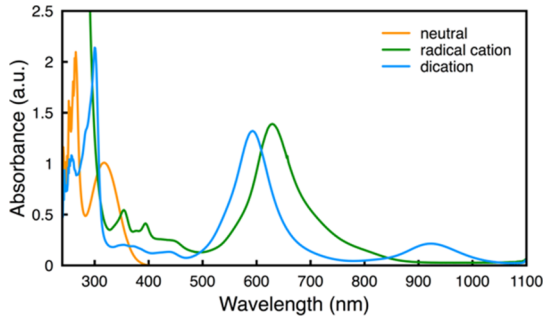

Figure 3. UV−vis absorption spectra of the neutral, radical cation, and dication forms of B(MEEO)EPT in ACN.

Table 1. Measured Redox Potentials, Peak Separations, and Peak-Current Ratios for the First and Second Oxidations, and Diffusion Coefficients of Neutral EPT, MEEPT, DMeOEPT, DMeOMEEPT, and B(MEEO)EPT[a]

compound	first oxidation			second oxidation			diffusion
	potential (V vs. $Cp_2Fe^{0/+}$)	peak separation (mV)	peak current ratio ($i_{p,ox}/i_{p,red}$)	potential (V vs. $Cp_2Fe^{0/+}$)	peak separation (mV)	peak current ratio ($i_{p,ox}/i_{p,red}$)	coefficient ($\times 10^{-6}$ cm^2 s^{-1})
EPT	0.278 ± 0.001	61 ± 1	1.00 ± 0.01	0.956 ± 0.002	68 ± 6	0.57 ± 0.09	2.3 ± 0.1
MEEPT	0.311 ± 0.001	61 ± 1	1.00 ± 0.01	0.937 ± 0.002	79 ± 2	0.26 ± 0.02	1.6 ± 0.1
DMeOEPT	0.056 ± 0.001	60 ± 1	0.99 ± 0.01	0.655 ± 0.001	60 ± 1	1.01 ± 0.01	1.8 ± 0.1
DMeOMEEPT	0.093 ± 0.001	60 ± 1	0.99 ± 0.02	0.666 ± 0.001	60 ± 1	0.90 ± 0.05	1.6 ± 0.1
B(MEEO)EPT	0.064 ± 0.001	61 ± 1	1.02 ± 0.04	0.654 ± 0.001	61 ± 1	1.01 ± 0.01	0.8 ± 0.1

[a]All cyclic voltammetry experiments were performed at 1 mM active material concentration. The peak separations and peak-current ratios were calculated at a scan rate of 10 mV s^{-1}. All measurements were performed in triplicate.

DOI: 10.1021/acs.chemmater.8b04770
Chem. Mater. 2019, 31, 4353−4363

spectra of the neutral, radical cation, and dication forms of DMeOMEEPT). Key features include a peak at 318 nm for the neutral compound; an intense peak at 629 nm and two sharp, less intense peaks at 354 and 394 nm for the radical cation; and peaks at 593 and 922 nm for the dication. These spectra are nearly identical to those of previously reported DMeOEPT,[39] which was expected due to the similarities in the electronic structure. To further support that the radical cation is being produced, we report the EPR spectrum of the radical cation in Figure S9. (The neutral and dication forms, which have no unpaired electrons, are EPR silent.)

The solubilities of the neutral, radical cation, and dication forms of DMeOMEEPT and B(MEEO)EPT were compared in 0.5 M $TEABF_4$/ACN and in 0.5 M TEATFSI/ACN (see Tables S1 and 2). We selected 0.5 M TEATFSI/ACN for flow

Table 2. Solubilities of the Neutral Molecules, Their Tetrafluoroborate Radical Cation Salts, and Their Bis(tetrafluoroborate) Dication Salts of DMeOEPT, DMeOMEEPT, and B(MEEO)EPT in 0.5 M TEATFSI/ACN, and for the Neutral Molecules and Radical Cations of EPT and MEEPT[a]

compound	neutral species (M)	radical cation (M)	dication (M)
EPT	0.10 ± 0.01	0.28 ± 0.01	[b]
MEEPT	miscible	0.40 ± 0.01	[b]
DMeOEPT	0.05 ± 0.01	0.06 ± 0.01	0.05 ± 0.01
DMeOMEEPT	miscible	0.11 ± 0.01	0.10 ± 0.01
B(MEEO)EPT	miscible	0.55 ± 0.01	0.54 ± 0.01

[a]The radical cation salts and the dication salts had tetrafluoroborate (BF_4^-) as a counterion. Solubility values are reported in molarity (M). [b]Dication data are not included for EPT and MEEPT, as they were not stable enough to isolate.

cell experiments because of the higher solubility of the neutral and charged states with the $TFSI^-$ salt. Although DMeOEPT is a solid at room temperature, the oligoglycol groups in the new materials lower their melting points and impart greater solubility. Both neutral compounds are liquids at room temperature and are miscible in nonaqueous electrolytes. The radical cation and dication salts of both compounds are solids, with lower solubilities than the miscible neutral forms. With two glycol chains, the solubility of the radical cation and dication forms of B(MEEO)EPT (0.55 and 0.54 M) is higher than those of the charged forms of DMeOMEEPT (0.11 and 0.10 M) (Table 2). Because of the combination of higher solubility of both oxidized forms as well as greater reversibility of the first and second oxidation events, we elected to use B(MEEO)EPT in flow cell experiments.

With B(MEEO)EPT selected for flow cell cycling studies, it was necessary to scale up the synthesis of this material in its radical cation form as the starting point on both sides of the symmetric flow cell. Thus, we scaled up the synthesis of the tetrafluoroborate radical cation salt of B(MEEO)EPT, performing reactions in batches as large as 8 g (mass of isolated material), again using $NOBF_4$ as the chemical oxidant. To confirm the identity of the radical cation salt, we crystallized the expected product, B(MEEO)EPT-BF_4, and analyzed resultant crystals using X-ray diffraction (experimental procedure available in the SI). The thermal ellipsoid plot obtained from X-ray experiments is shown in Figure 4. Notably, the isolation of this salt as X-ray quality single crystals

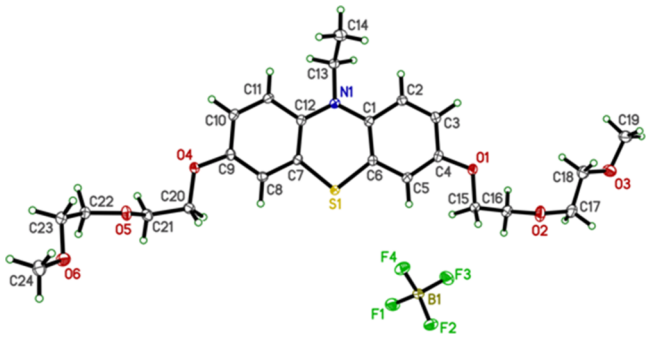

Figure 4. Thermal ellipsoid plot of B(MEEO)EPT-BF_4 obtained from single-crystal X-ray diffraction experiments from the scaled-up synthesis.

not only provides proof of structural assignment but also demonstrates the stability of this organic radical cation.

Flow Cell Cycling. Symmetric flow cells offer many benefits when evaluating soluble redox-active materials under flow battery relevant conditions.[4,38,59] All states of charge of a single redox couple can be accessed, the possibility of contamination from a counter electrode is removed, and the flowing electrolyte increases mass transfer through the porous electrodes, allowing for higher active material concentrations and current densities to be employed. Here, we used a symmetric cell configuration to investigate rate capabilities and cycle stability of B(MEEO)EPT across all three oxidation states. In the case of symmetric cells utilizing one-electron donors, two different states of charge are accessed in each chamber: the neutral species, P, and the radical cation, $P^{\bullet+}$. However, when two-electron-donating active species are studied, three different states of charge are accessible; so in addition to the neutral species and the radical cation, the dication, P^{2+}, is also present (Figure 5a). In an ideal constant current cycling experiment for a two-electron donor, two unique potential plateaus occur at overpotentials of equal magnitude and opposite sign, with each plateau corresponding to 50% of the total charge capacity (Figure 5b). Therefore, at 50% state of charge, a sharp increase (charging) or decrease (discharging) in the potential occurs. When charging begins, P is oxidized to $P^{\bullet+}$ on one side of the cell and P^{2+} is simultaneously reduced to $P^{\bullet+}$ on the other side, leading to the first voltage plateau. Once P and P^{2+} are depleted, both tanks contain only $P^{\bullet+}$. At this point, $P^{\bullet+}$ is oxidized to P^{2+} on one side of the cell and is reduced to P on the other side, leading to the second plateau. During discharge, the reverse reactions occur, again leading to two distinct voltage plateaus.

An imbalanced cell can result from a mismatch in the electrolyte volume on each side of the cell (e.g., from crossover) and/or from a mismatch in respective active species concentrations. This phenomenon may be a result of cell polarization and species crossover that is exacerbated by the use of a nonselective separator. Specifically, as the current density increases, the cell will reach the prescribed voltage cutoff before all of the molecules have been oxidized or reduced leaving mixtures of $P/P^{\bullet+}$ and $P^{\bullet+}/P^{2+}$ on either side of the cell, which, in turn, will present as a third voltage plateau on subsequent charge and discharge cycles (Figure 5c). This behavior is further complicated and compounded by active species crossover between the two electrolytes. If the amount of P on one side of the cell is less than the amount of P^{2+} on the other side, upon complete oxidation of P to $P^{\bullet+}$, an excess

DOI: 10.1021/acs.chemmater.8b04770
Chem. Mater. 2019, 31, 4353−4363

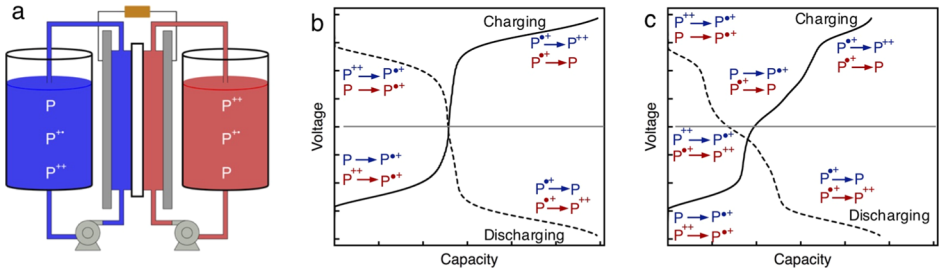

Figure 5. Schematic of a symmetric flow cell showing the states of charge accessed for a given molecule, P, with three stable oxidation states (a), and the corresponding charging (solid line) and discharging (dotted line) potential profiles for constant current cycling labeled with the electrochemical reactions corresponding to each voltage plateau in a balanced cell (b) and an imbalanced cell (c).

of P^{2+} will remain unreduced on the opposite side (Figure 5c). An example of a voltage profile in this scenario is shown in Figure 5c during both charge and discharge. The expected cell voltage is 0 V because the reaction is cycling against itself.[38] The capacity of this middle plateau is dependent on the amount of excess active material (whether P or P^{2+}) present on one side of the cell. Note that a third plateau also forms if the reduction of P^{2+} to $P^{\bullet+}$ was the limiting reaction. The formation of this new voltage plateau emphasizes a challenge with two-electron-transfer molecules and the importance of preventing crossover during cell operation because a mismatch in active species concentration not only reduces the accessed capacity but also alters the voltage profile observed during cell cycling.

Several approaches can allow for the configuration of a balanced symmetric cell before starting charge/discharge cycling. These include (i) loading equal volumes of two separate, equimolar of solutions of P and P^{2+}, (ii) premixing P and P^{2+} in a 1:1 ratio, dividing the resulting solution into two equivalent volumes, and then pre-charging the cell to reduce $P^{\bullet+}$ to P on one side and oxidize $P^{\bullet+}$ to P^{2+} on the other side, or (iii) dividing a solution of only $P^{\bullet+}$ into two equivalent volumes and then pre-charging the cell to reduce and oxidize to P and P^{2+}, respectively. Here, we employ the third approach for the convenience of a single starting material and due to the challenges of preventing electrolyte mixing across the non-selective separator during cell start-up.

We first performed a variable rate experiment to determine the tradeoff between applied current density, overpotential, and accessed capacity with a secondary goal of identifying an appropriate current density for analyzing the B(MEEO)EPT stability in symmetric cells. Thus, we conducted a rate study, cycling cells containing B(MEEO)EPT for five cycles each at current densities of 10, 20, 30, 40, and 50 mA cm^{-2}, followed by five more cycles at 10 mA cm^{-2}, the last of which was performed to determine whether accessing the higher current densities adversely impacts cell components (e.g., electrode degradation) and/or active material. The voltage versus capacity profiles for the fifth cycle at each current density are shown in Figure 6a, and the charge and discharge capacities with the Coulombic efficiencies are shown in Figure 6b. As expected, the accessed capacities decreased as current densities increase, which is due to the larger cell polarization present at high current densities. As evidenced by a comparison the 5th cycle in the first and last sets of 10 mA cm^{-2} cycles, the capacity faded by about 8% over the course of the 145 h experiment which we tentatively attribute to the emergence of a third voltage plateau centered around 0 V (see Table 3).

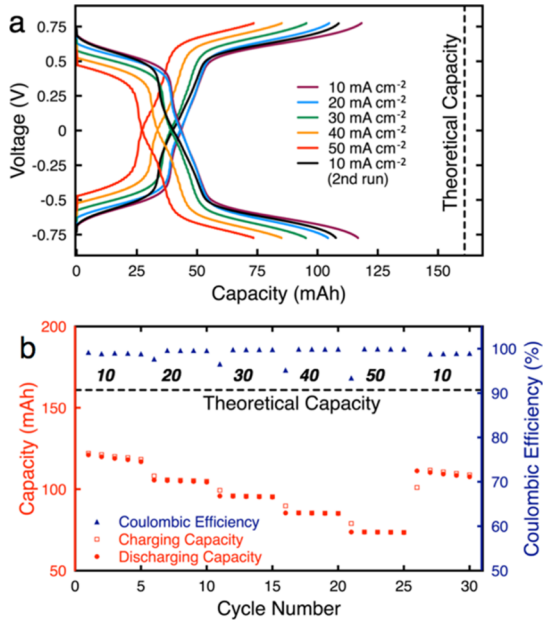

Figure 6. Rate study of B(MEEO)EPT cycling in a symmetric flow cell, showing the potential vs capacity (a) and the capacity vs cycling number (b) at various applied current densities. The numerical values below each Coulombic efficiency segment represent the applied current densities in mA cm^{-2}. The potential cutoffs for each flow cell experiment were ±0.775 V. In both figures, a dashed black line is drawn to represent the theoretical capacity (161 mA h). The total experimental run time was 145 h.

Table 3 highlights the additional tradeoff between the current density and the charging/discharging efficiency. The difference in accessed capacity of the two voltage plateaus observed in the voltage versus capacity profiles in Figure 6a and Table 3 shows a deviation from the idealized behavior illustrated in Figure 5b. The percent of charging and discharging capacity accessed at each plateau is calculated by identifying the maximum (charging) or minimum (discharging) in the derivative of the voltage profile as each extreme represents the transition from one redox plateau to another.[60] For reference, in the ideal case, the capacity would be split evenly between the low- and high-voltage plateaus with no intermediate voltage plateaus.

Two notable trends are observed in Table 3. First, as anticipated, the lower current densities—thus longest cycles—showed the lower coulombic efficiencies, albeit only 1.0−1.1% lower than the shortest cycle. We attribute this minor inefficiency to in-cycle active species crossover and self-discharge through the nonselective separator. Second, in

DOI: 10.1021/acs.chemmater.8b04770
Chem. Mater. 2019, 31, 4353−4363

Table 3. Percent of the Charging and Discharging Capacity Accessed on Each Potential Plateau during Charging and Discharging and the Corresponding Accessed Capacity and Coulombic Efficiency for Each of the Current Densities Examined, Obtained from the Variable-Rate Cycling Data Shown in Figure 6[a]

	charging			discharging				
current density (mA cm^{-2})	lower plateau (%)	middle plateau (%)	upper plateau (%)	lower plateau (%)	middle plateau (%)	upper plateau (%)	accessed capacity (%)	coulombic efficiency (%)
10	33.3 ± 0.2	9.6 ± 0.2	57.1 ± 0.4	56.5 ± 0.2	9.4 ± 0.3	34.1 ± 0.1	73.5	98.8
20	37.5 ± 0.3	10.7 ± 0.3	51.8 ± 0.1	51.7 ± 0.1	10.6 ± 0.1	37.7 ± 0.1	65.1	99.5
30	37.8 ± 0.4	11.9 ± 0.1	50.3 ± 0.3	50.2 ± 0.1	11.8 ± 0.1	38.0 ± 0.1	59.2	99.8
40	36.9 ± 0.7	13.6 ± 0.1	49.5 ± 0.4	49.7 ± 0.1	13.1 ± 0.1	37.2 ± 0.1	52.9	99.9
50	35.5 ± 0.8	14.0 ± 0.4	51 ± 1	51.5 ± 0.2	14.9 ± 0.5	33.6 ± 0.6	45.6	99.9
10	30 ± 2	14.9 ± 0.4	55 ± 2	52.9 ± 0.2	14.6 ± 0.4	32.5 ± 0.1	67.6	98.9

[a]The data corresponds to the average of each charging/discharging cycle.

general, the active materials appear to spend more time in the extreme voltage plateaus. A similar but simpler case (i.e., no convection) of this behavior would be voltage profiles associated with Sand's time measurements for different oxidation states of multiple electron-transfer materials.[60] If translated to full redox flow cell operation (e.g., second redox couple at a disparate voltage), this observation suggests lower voltage efficiencies and consequently reduced energy efficiencies. Indeed, similar observations were made by Laramie et al. when studying two-electron-transfer molecules in a full cell.[61] We note that there does not appear to be a current density dependence of this trend over the relatively narrow range of current densities explored which is also in agreement with the Sand's time analysis.[60] More broadly, this inefficiency is intrinsic to materials with multiple, independent electron-transfer events, suggesting that, in principle, greater volumetric capacities are achievable but with a concomitant penalty in voltaic efficiency. A quantitative description of this trade-off is beyond the scope of the present work but will be addressed in the future.

Constant current symmetric cell cycling was then performed to evaluate the long-term stability of B(MEEO)EPT. Here, a symmetric cell was assembled with each half cell containing 10 mL of solution containing 0.3 M B(MEEO)EPT (0.6 M faradaic concentration) in 0.5 M TEATFSI in ACN, and cycling was performed at 25 mA cm^{-2}. This current density was chosen to balance experimental runtime (roughly 2 h for each half cycle) and fraction of the capacity accessed per cycle. Figure 7a shows the voltage versus capacity profiles for the charge and discharge of select cycles. The charge and discharge capacities and coulombic efficiencies for each cycle are shown in Figure 7b.

In this cycling experiment, about 80% of the theoretical capacity was accessed initially, which is larger than expected based on the rate study and tentatively attributed to variability in the cell build (i.e., slightly lower area specific resistance) and the initial symmetry of the cell (i.e., no start-up or operation-induced electrolyte misbalance). Over the course of the experiment (460 h), a 27% capacity fade was observed. For the first 85 cycles (300 h), the capacity faded at a rate of ca. 0.1% per cycle, whereas for cycles 86−140, the average fade rate increased to ca. 0.4% per cycle. We hypothesize that the majority of this performance decay is due to the combination of cell polarization and active species crossover, rather than material degradation, and thus may ultimately be reversible. This hypothesis is supported by the appearance and growth of a new voltage plateau around 0 V over the course of the experiment (Figure 5c). Indeed, by cycle 140, the capacity

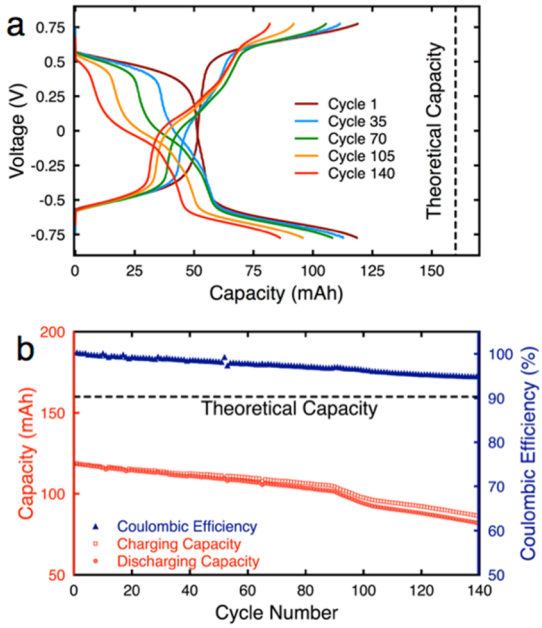

Figure 7. Constant current cycling of B(MEEO)EPT in a symmetric flow cell at 25 mA cm^{-2} accessing both electron-transfer events: capacity vs potential (a), charging (red, square) and discharging (red, circle), as well as the Coulombic efficiencies (blue, triangle) as a function of cycle number (b). The potential cutoffs imposed during the flow cell experiment were ±0.775 V. The theoretical capacity (dashed black line) is 16.1 A h L^{-1} (161 mA h), and the total experimental runtime was 460 h.

accessed on this middle plateau was near equal to that accessed on the lower plateau and greater than that of the upper potential plateau. As the new plateau continued to increase, the accessed capacity decreased because more B(MEEO)EPT$^{\bullet+}$ remains either unoxidized or unreduced on one side of the cell. In addition, at the end of the experiment, unequal solution volumes were observed in the two electrolyte chambers, which is evidence of a capacity-limiting electrolyte imbalance.

Post-Test Analyses. To determine whether the observed capacity loss was due to limitations in cell assembly and operation as opposed to active species decomposition, we analyzed the cycled positive and negative electrolyte solutions using microelectrode voltammetry (Figure 8a) and UV−vis absorption spectroscopy (Figure 8b). Microelectrode voltammetry was employed because it enables direct electrolyte analysis without dilution. Moreover, the presence (or absence) of individual species as well as their relative concentrations in the electrolyte solutions can be extracted from the steady-state

DOI: 10.1021/acs.chemmater.8b04770
Chem. Mater. 2019, 31, 4353−4363

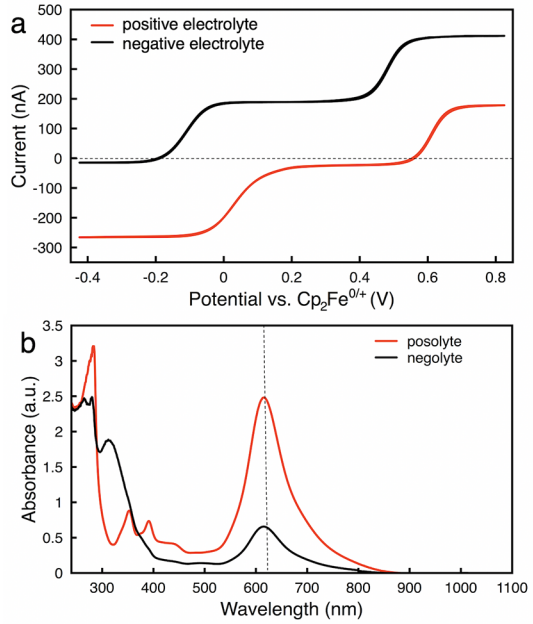

Figure 8. Carbon fiber microelectrode cyclic voltammetry scans (10 mV s^{-1}) of the positive electrolyte (red) and negative electrolyte (black) after symmetric cell cycling at 0.3 M in active material (a) and corresponding UV−vis absorption spectra (b). For UV−vis measurements, the working solutions were diluted 1000× to reach an estimated total species concentration of 0.3 mM, assuming equal species distribution across the negative electrolyte and positive electrolyte and no decomposition of B(MEEO)EPT into a new molecular species.

voltammetric response.[60] Three current plateaus were present in each microelectrode voltammogram where the lowest voltage (most negative) plateau corresponds to the neutral form of B(MEEO)EPT, the middle plateau to the radical cation, and the highest plateau to the dication. The plateau closest to a *y*-axis value of zero represents the highest concentration species in the solution. The cell was stopped and disassembled in the charged state; therefore, the positive electrolyte as defined by the electrolyte connected to the working electrode should ideally contain only P^{2+}, whereas the negative electrolyte (counter electrode) ideally would only contain P.

From the microelectrode CV, the dominant species in the positive electrolyte and negative electrolyte are the radical cation and the neutral compound, respectively. Further, for the negative electrolyte, there is a slight reducing current at the lowest potentials used (i.e., on the plateau corresponding to the neutral species), indicating that there is either radical cation or dication or both present. However, it is likely that any dication in solution would react with the excess neutral species, only leaving the radical cation and neutral species. Similarly, for the positive electrolyte, there is a slight negative current at the intermediate potentials (i.e., on the plateau corresponding to the radical cation), implying that there is some dication in solution that can be reduced. In both cases, on the basis of the relative current magnitudes, we can deduce that the majority species in each solution are at least an order of magnitude greater concentration than the minority species, but quantitative assessment of minority species concentrations required knowledge of species-specific diffusion coefficients. Thus, we can conclude that there is at least radical cation and dication in the positive electrolyte and at least neutral species and one oxidized species in the negative electrolyte, and it is possible that more species are also present (neutral in the positive electrolyte and dication in the negative electrolyte). In Figure 8b, the UV−vis spectra show the presence of radical cation in the positive electrolyte and a combination of neutral compound and radical cation in the negative electrolyte. We see no evidence of active species decomposition in the UV−vis spectra, suggesting that this is not the source of capacity fade. Further, we do not see any signature of the dication in the UV−vis absorption spectra, which were obtained about a week after microelectrode voltammetry experiments. We hypothesize that homogeneous disproportionation reactions, between the dication and neutral compound to produce two radical cations, occur continuously postmortem which would explain the lower dication concentration in Figure 8a and the lack of dication in Figure 8b.

CONCLUSIONS

In summary, we report two new, two-electron-donating phenothiazine derivatives in which solubility and stability of the neutral, radical cation, and dication forms in a nonaqueous electrolyte are significantly increased compared to previous phenothiazine derivatives. By introducing one or two oligoglycol chains on the periphery of a less soluble two-electron-donating core, the solubility of the new derivatives is improved to a point similar to that of the previously reported one-electron donor (MEEPT), miscible with 0.5 M TEATFSI/ACN in its neutral form. In particular, for B(MEEO)EPT, the increase in molecular weight by a factor of 1.5 compared to one-electron-donating MEEPT is offset by a doubling in electron storage capacity per phenothiazine unit without compromising solubility. However, a 0.6 V gap still exists between the electron transfer events leading to additional charging/discharging inefficiencies, which will need to be reduced to limit operation losses. B(MEEO)EPT is sufficiently soluble in all three states of charge as to allow for symmetric flow cell cycling experiments at concentrations of 0.3 M (0.6 M faradaic concentration). During long-term symmetric cell cycling, B(MEEO)EPT cycled for 460 h with ca. 30% capacity fade.

Importantly, although capacity fade is observed, our experimental results indicate that this is due to limitations in our experimental apparatus, specifically the use of a non-selective separator, rather than decomposition of the redox couple. The evolution of the voltage profile observed during cycling is consistent with active species crossover as evidenced by both the appearance of a new voltage plateau at around 0 V and the imbalanced electrolytes at the end of the experiment. Moreover, the results from combined microelectrode and UV−vis analyses of cycled electrolytes suggest that the coulombic inefficiencies are mostly due to self-discharge of the dication form of B(MEEO)EPT through electron-transfer reactions, potentially a reaction with the neutral species. As such, if suitable conductive and selective separators were employed, we anticipate that more extensive cycling could be realized with B(MEEO)EPT. More broadly, though further improvements in the phenothiazine derivatives to increase redox potentials and reduce the voltage gap between electron transfer events will ultimately be necessary to realize high-voltage nonaqueous RFBs, this study represents an important example of multiproperty tuning of organic molecules for charge storage. Although the functionalization strategies reported here are

DOI: 10.1021/acs.chemmater.8b04770
Chem. Mater. 2019, 31, 4353−4363

targeted to phenothiazine derivatives in electrolytes based on polar aprotic solvents, the design ethos and approach outlined are generalizable and can be applied to other organic redox materials for use in electrochemical technologies.

■ ASSOCIATED CONTENT

Supporting Information

The Supporting Information is available free of charge on the ACS Publications website at DOI: 10.1021/acs.chemmater.8b04770.

Crystallographic data of (B(MEEO)EPT) (PDF)

Crystallographic data of (B(MEEO)EPT) (CIF)

General information about materials and analysis as well as synthetic procedures and additional solubility data and plots of ^{1}H and ^{13}C NMR spectra, UV−vis spectra, EPR spectra, and cyclic voltammograms at various scan rates with Randles−Sevcik plots (PDF)

■ AUTHOR INFORMATION

Corresponding Authors

*E-mail: brushett@mit.edu (F.R.B.).

*E-mail: susan.odom@uky.edu (S.A.O.).

ORCID

Matthew D. Casselman: 0000-0001-9040-4663

Sean R. Parkin: 0000-0001-5777-3918

Fikile R. Brushett: 0000-0002-7361-6637

Susan A. Odom: 0000-0001-6708-5852

Author Contributions

⊥N.H.A. and J.A.K. contributed equally to the manuscript.

Notes

The authors declare no competing financial interest.

■ ACKNOWLEDGMENTS

This work was funded by the National Science Foundation's Division of Chemistry (award 1300653) and EPSCoR Program (award 1355438), and through the Department of Energy, Office of Basic Science through an Energy Innovation Hub: Joint Center for Energy Storage Research (JCESR). We thank Andrew Hipsley for assistance in the acquisition of EPR spectra. Crystallographic work was supported by the NSF MRI program (awards CHE-0319176 and CHE-1625732).

■ REFERENCES

(1) Denholm, P.; Ela, E.; Kirby, B.; Milligan, M. *The Role of Energy Storage with Renewable Electricity Generation*; National Renewable Energy Laboratory, 2010.

(2) Gyuk, I.; Johnson, M.; Vetrano, J.; Lynn, K.; Parks, W.; Handa, R.; Kannberg, L.; Hearne, S.; Waldrip, K.; Braccio, R. *Grid Energy Storage*; US Department of Energy: Washington DC, 2013.

(3) Huskinson, B.; Marshak, M. P.; Suh, C.; Er, S.; Gerhardt, M. R.; Galvin, C. J.; Chen, X.; Aspuru-Guzik, A.; Gordon, R. G.; Aziz, M. J. A Metal-Free Organic-Inorganic Aqueous Flow Battery. *Nature* **2014**, *505*, 195−198.

(4) Milshtein, J. D.; Kaur, A. P.; Casselman, M. D.; Kowalski, J. A.; Modekrutti, S.; Zhang, P. L.; Harsha Attanayake, N.; Elliott, C. F.; Parkin, S. R.; Risko, C.; Brushett, F. R.; Odom, S. A. High Current Density, Long Duration Cycling of Soluble Organic Active Species for Non-Aqueous Redox Flow Batteries. *Energy Environ. Sci.* **2016**, *9*, 3531−3543.

(5) Jia, C.; Pan, F.; Zhu, Y. G.; Huang, Q.; Lu, L.; Wang, Q. High-energy density nonaqueous all redox flow lithium battery enabled with a polymeric membrane. *Sci. Adv.* **2015**, *1*, No. e1500886.

(6) Reynard, D.; Dennison, C. R.; Battistel, A.; Girault, H. H. Efficiency Improvement of an All-Vanadium Redox Flow Battery by Harvesting Low-Grade Heat. *J. Power Sources* **2018**, *390*, 30−37.

(7) Kwabi, D. G.; Lin, K.; Ji, Y.; Kerr, E. F.; Goulet, M.-A.; De Porcellinis, D.; Tabor, D. P.; Pollack, D. A.; Aspuru-Guzik, A.; Gordon, R. G.; Aziz, M. J. Alkaline Quinone Flow Battery with Long Lifetime at pH 12. *Joule* **2018**, *2*, 1894−1906.

(8) Duan, W.; Huang, J.; Kowalski, J. A.; Shkrob, I. A.; Vijayakumar, M.; Walter, E.; Pan, B.; Yang, Z.; Milshtein, J. D.; Li, B.; Liao, C.; Zhang, Z.; Wang, W.; Liu, J.; Moore, J. S.; Brushett, F. R.; Zhang, L.; Wei, X. "Wine-Dark Sea" in an Organic Flow Battery: Storing Negative Charge in 2,1,3-Benzothiadiazole Radicals Leads to Improved Cyclability. *ACS Energy Lett.* **2017**, *2*, 1156−1161.

(9) Wei, X.; Xu, W.; Vijayakumar, M.; Cosimbescu, L.; Liu, T.; Sprenkle, V.; Wang, W. TEMPO-Based Catholyte for High-Energy Density Nonaqueous Redox Flow Batteries. *Adv. Mater.* **2014**, *26*, 7649−7653.

(10) Gong, K.; Fang, Q.; Gu, S.; Li, S. F. Y.; Yan, Y. Nonaqueous Redox-Flow Batteries: Organic Solvents, Supporting Electrolytes, and Redox Pairs. *Energy Environ. Sci.* **2015**, *8*, 3515−3530.

(11) Kwon, G.; Lee, S.; Hwang, J.; Shim, H.-S.; Lee, B.; Lee, M. H.; Ko, Y.; Jung, S.-K.; Ku, K.; Hong, J.; Kang, K. Multi-redox Molecule for High-Energy Redox Flow Batteries. *Joule* **2018**, *2*, 1771−1782.

(12) Parasuraman, A.; Lim, T. M.; Menictas, C.; Skyllas-Kazacos, M. Review of material research and development for vanadium redox flow battery applications. *Electrochim. Acta* **2013**, *101*, 27−40.

(13) Alotto, P.; Guarnieri, M.; Moro, F. Redox Flow Batteries for the Storage of Renewable Energy: A Review. *Renew. Sustain. Energy Rev.* **2014**, *29*, 325−335.

(14) Kaur, A. P.; Holubowitch, N. E.; Ergun, S.; Elliott, C. F.; Odom, S. A. A Highly Soluble Organic Catholyte for Non-aqueous Redox Flow Batteries. *Energy Technol.* **2015**, *3*, 476−480.

(15) Darling, R. M.; Gallagher, K. G.; Kowalski, J. A.; Ha, S.; Brushett, F. R. Pathways to Low-Cost Electrochemical Energy Storage: A Comparison of Aqueous and Nonaqueous Flow Batteries. *Energy Environ. Sci.* **2014**, *7*, 3459−3477.

(16) Dmello, R.; Milshtein, J. D.; Brushett, F. R.; Smith, K. C. Cost-driven Materials Selection Criteria for Redox Flow Battery Electrolytes. *J. Power Sources* **2016**, *330*, 261−272.

(17) Oriji, G.; Katayama, Y.; Miura, T. Investigation on V(IV)/V(V) Species in a Vanadium Redox Flow Battery. *Electrochim. Acta* **2004**, *49*, 3091−3095.

(18) Rahman, F.; Skyllas-Kazacos, M. Vanadium redox battery: Positive half-cell electrolyte studies. *J. Power Sources* **2009**, *189*, 1212−1219.

(19) Li, B.; Li, L.; Wang, W.; Nie, Z.; Chen, B.; Wei, X.; Luo, Q.; Yang, Z.; Sprenkle, V. Fe/V Redox Flow Battery Electrolyte Investigation and Optimization. *J. Power Sources* **2013**, *229*, 1−5.

(20) Xu, Q.; Zhao, T. S.; Wei, L.; Zhang, C.; Zhou, X. L. Electrochemical Characteristics and Transport Properties of Fe(II)/Fe(III) Redox Couple in a Non-aqueous Reline Deep Eutectic Solvent. *Electrochim. Acta* **2015**, *154*, 462−467.

(21) Hwang, S.; Kim, H.-S.; Ryu, J. H.; Oh, S. M. Ni(II)-Chelated Thio-crown Complex as a Single Redox Couple for Non-Aqueous Flow Batteries. *Electrochem. Commun.* **2017**, *85*, 36−39.

(22) Stauber, J. M.; Zhang, S.; Gvozdik, N.; Jiang, Y.; Avena, L.; Stevenson, K. J.; Cummins, C. C. Cobalt and Vanadium Trimetaphosphate Polyanions: Synthesis, Characterization, and Electrochemical Evaluation for Non-aqueous Redox-Flow Battery Applications. *J. Am. Chem. Soc.* **2018**, *140*, 538−541.

(23) Cabrera, P. J.; Yang, X.; Suttil, J. A.; Brooner, R. E. M.; Thompson, L. T.; Sanford, M. S. Evaluation of Tris-Bipyridine Chromium Complexes for Flow Battery Applications: Impact of Bipyridine Ligand Structure on Solubility and Electrochemistry. *Inorg. Chem.* **2015**, *54*, 10214−10223.

(24) Sleightholme, A. E. S.; Shinkle, A. A.; Liu, Q.; Li, Y.; Monroe, C. W.; Thompson, L. T. Non-aqueous Manganese Acetylacetonate Electrolyte for Redox Flow Batteries. *J. Power Sources* **2011**, *196*, 5742−5745.

DOI: 10.1021/acs.chemmater.8b04770
Chem. Mater. 2019, 31, 4353−4363

(25) Hu, B.; DeBruler, C.; Rhodes, Z.; Liu, T. L. Long-Cycling Aqueous Organic Redox Flow Battery (AORFB) toward Sustainable and Safe Energy Storage. *J. Am. Chem. Soc.* **2017**, *139*, 1207−1214.
(26) DeBruler, C.; Hu, B.; Moss, J.; Luo, J.; Liu, T. L. A Sulfonate-Functionalized Viologen Enabling Neutral Cation Exchange, Aqueous Organic Redox Flow Batteries toward Renewable Energy Storage. *ACS Energy Lett.* **2018**, *3*, 663−668.
(27) Hollas, A.; Wei, X.; Murugesan, V.; Nie, Z.; Li, B.; Reed, D.; Liu, J.; Sprenkle, V.; Wang, W. A Biomimetic High-capacity Phenazine-Based Anolyte for Aqueous Organic Redox Flow Batteries. *Nat. Energy* **2018**, *3*, 508−514.
(28) Huang, J.; Yang, Z.; Vijayakumar, M.; Duan, W.; Hollas, A.; Pan, B.; Wang, W.; Wei, X.; Zhang, L. A Two-Electron Storage Nonaqueous Organic Redox Flow Battery. *Adv. Sustainable Syst.* **2018**, *2*, 1700131−1700137.
(29) Zhang, J.; Shkrob, I. A.; Assary, R. S.; Tung, S. o.; Silcox, B.; Curtiss, L. A.; Thompson, L.; Zhang, L. Toward Improved Catholyte Materials for Redox Flow Batteries: What Controls Chemical Stability of Persistent Radical Cations? *J. Phys. Chem. C* **2017**, *121*, 23347−23358.
(30) Winsberg, J.; Hagemann, T.; Janoschka, T.; Hager, M. D.; Schubert, U. S. Redox-Flow Batteries: From Metals to Organic Redox-Active Materials. *Angew. Chem., Int. Ed.* **2017**, *56*, 686−711.
(31) Leung, P.; Shah, A. A.; Sanz, L.; Flox, C.; Morante, J. R.; Xu, Q.; Mohamed, M. R.; Ponce de León, C.; Walsh, F. C. Recent Developments in Organic Redox Flow Batteries: A Critical Review. *J. Power Sources* **2017**, *360*, 243−283.
(32) Quan, M.; Sanchez, D.; Wasylkiw, M. F.; Smith, D. K. Voltammetry of Quinones in Unbuffered Aqueous Solution: Reassessing the Roles of Proton Transfer and Hydrogen Bonding in the Aqueous Electrochemistry of Quinones. *J. Am. Chem. Soc.* **2007**, *129*, 12847−12856.
(33) Cao, J.; Tao, M.; Chen, H.; Xu, J.; Chen, Z. A Highly Reversible Anthraquinone-based Anolyte for Alkaline aqueous Redox Flow Batteries. *J. Power Sources* **2018**, *386*, 40−46.
(34) Yang, Z.; Tong, L.; Tabor, D. P.; Beh, E. S.; Goulet, M.-A.; De Porcellinis, D.; Aspuru-Guzik, A.; Gordon, R. G.; Aziz, M. J. Alkaline Benzoquinone Aqueous Flow Battery for Large-Scale Storage of Electrical Energy. *Adv. Energy Mater.* **2018**, *8*, 1702056.
(35) Beh, E. S.; De Porcellinis, D.; Gracia, R. L.; Xia, K. T.; Gordon, R. G.; Aziz, M. J. A Neutral pH Aqueous Organic-Organometallic Redox Flow Battery with Extremely High Capacity Retention. *ACS Energy Lett.* **2017**, *2*, 639−644.
(36) Armstrong, C. G.; Toghill, K. E. Cobalt(II) complexes with azole-pyridine type ligands for non-aqueous redox-flow batteries: Tunable electrochemistry via structural modification. *J. Power Sources* **2017**, *349*, 121−129.
(37) Hudak, N. S.; Small, L. J.; Pratt, H. D.; Anderson, T. M. Through-Plane Conductivities of Membranes for Nonaqueous Redox Flow Batteries. *J. Electrochem. Soc.* **2015**, *162*, A2188−A2194.
(38) Milshtein, J. D.; Barton, J. L.; Darling, R. M.; Brushett, F. R. 4-Acetamido-2,2,6,6-tetramethylpiperidine-1-oxyl as a Model Organic Redox Active Compound for Nonaqueous Flow Batteries. *J. Power Sources* **2016**, *327*, 151−159.
(39) Kowalski, J. A.; Casselman, M. D.; Kaur, A. P.; Milshtein, J. D.; Elliott, C. F.; Modekrutti, S.; Attanayake, N. H.; Zhang, N.; Parkin, S. R.; Risko, C.; Brushett, F. R.; Odom, S. A. A Stable Two-Electron-Donating Phenothiazine for Application in Nonaqueous Redox Flow Batteries. *J. Mater. Chem. A* **2017**, *5*, 24371−24379.
(40) Chakrabarti, M. H.; Dryfe, R. A. W.; Roberts, E. P. L. Evaluation of Electrolytes for Redox Flow Battery Applications. *Electrochim. Acta* **2007**, *52*, 2189−2195.
(41) Ding, Y.; Zhao, Y.; Li, Y.; Goodenough, J. B.; Yu, G. A High-Performance all-Metallocene-based, Non-Aqueous Redox Flow Battery. *Energy Environ. Sci.* **2017**, *10*, 491−497.
(42) Vangelder, L. E.; Kosswattaarachchi, A. M.; Forrestel, P. L.; Cook, T. R.; Matson, E. M. Polyoxovanadate-Alkoxide Clusters as Multi-Electron Charge Carriers for Symmetric Non-aqueous Redox Flow Batteries. *Chem. Sci.* **2018**, *9*, 1692−1699.
(43) Doris, S. E.; Ward, A. L.; Baskin, A.; Frischmann, P. D.; Gavvalapalli, N.; Chénard, E.; Sevov, C. S.; Prendergast, D.; Moore, J. S.; Helms, B. A. Macromolecular Design Strategies for Preventing Active-Material Crossover in Non-Aqueous All-Organic Redox-Flow Batteries. *Angew. Chem., Int. Ed.* **2017**, *56*, 1595−1599.
(44) Hendriks, K. H.; Robinson, S. G.; Braten, M. N.; Sevov, C. S.; Helms, B. A.; Sigman, M. S.; Minteer, S. D.; Sanford, M. S. High-Performance Oligomeric Catholytes for Effective Macromolecular Separation in Nonaqueous Redox Flow Batteries. *ACS Cent. Sci.* **2018**, *4*, 189−196.
(45) Baran, M. J.; Braten, M. N.; Montoto, E. C.; Gossage, Z. T.; Ma, L.; Chénard, E.; Moore, J. S.; Rodríguez-López, J.; Helms, B. A. Designing Redox-Active Oligomers for Crossover-Free, Nonaqueous Redox-Flow Batteries with High Volumetric Energy Density. *Chem. Mater.* **2018**, *30*, 3861−3866.
(46) Montoto, E. C.; Cao, Y.; Hernández-Burgos, K.; Sevov, C. S.; Braten, M. N.; Helms, B. A.; Moore, J. S.; Rodríguez-López, J. Effect of the Backbone Tether on the Electrochemical Properties of Soluble Cyclopropenium Redox-Active Polymers. *Macromolecules* **2018**, *51*, 3539−3546.
(47) Montoto, E. C.; Nagarjuna, G.; Moore, J. S.; Rodríguez-López, J. Redox Active Polymers for Non-Aqueous Redox Flow Batteries: Validation of the Size-Exclusion Approach. *J. Electrochem. Soc.* **2017**, *164*, A1688−A1694.
(48) Pan, F.; Yang, J.; Jia, C.; Li, H.; Wang, Q. Biphenyl-lithium-TEGDME Solution as Anolyte for High Energy Density Non-aqueous Redox Flow Lithium Battery. *J. Energy Chem.* **2018**, *27*, 1362−1368.
(49) Wang, W.; Sprenkle, V. Redox flow batteries go organic. *Nat. Chem.* **2016**, *8*, 204.
(50) Sevov, C. S.; Hickey, D. P.; Cook, M. E.; Robinson, S. G.; Barnett, S.; Minteer, S. D.; Sigman, M. S.; Sanford, M. S. Physical Organic Approach to Persistent, Cyclable, Low-Potential Electrolytes for Flow Battery Applications. *J. Am. Chem. Soc.* **2017**, *139*, 2924−2927.
(51) Sevov, C. S.; Brooner, R. E. M.; Chénard, E.; Assary, R. S.; Moore, J. S.; Rodríguez-López, J.; Sanford, M. S. Evolutionary design of low molecular weight organic anolyte materials for applications in nonaqueous redox flow batteries. *J. Am. Chem. Soc.* **2015**, *137*, 14465−14472.
(52) Huang, J.; Su, L.; Kowalski, J. A.; Barton, J. L.; Ferrandon, M.; Burrell, A. K.; Brushett, F. R.; Zhang, L. A Subtractive Approach to Molecular Engineering of Dimethoxybenzene-Based Redox Materials for Non-aqueous Flow Batteries. *J. Mater. Chem. A* **2015**, *3*, 14971−14976.
(53) Wei, X.; Cosimbescu, L.; Xu, W.; Hu, J. Z.; Vijayakumar, M.; Feng, J.; Hu, M. Y.; Deng, X.; Xiao, J.; Liu, J.; Sprenkle, V.; Wang, W. Towards High-Performance Nonaqueous Redox Flow Electrolyte Via Ionic Modification of Active Species. *Adv. Energy Mater.* **2015**, *5*, 1400678.
(54) Wang, W.; Xu, W.; Cosimbescu, L.; Choi, D.; Li, L.; Yang, Z. Anthraquinone with Tailored Structure for a Nonaqueous Metal-Organic Redox Flow Battery. *Chem. Commun.* **2012**, *48*, 6669−6671.
(55) Li, S.; Xie, M.; Liu, J.; Wang, H.; Yan, H.; Wang, F.; Peng, S. Layer Structured Sulfur/Expanded Graphite Composite as Cathode for Lithium Battery. *Electrochem. Solid State Lett.* **2011**, *14*, A105−A173.
(56) Takechi, K.; Kato, Y.; Hase, Y. A Highly Concentrated Catholyte Based on a Solvate Ionic Liquid for Rechargeable Flow Batteries. *Adv. Mater.* **2015**, *27*, 2501−2506.
(57) Brushett, F. R.; Vaughey, J. T.; Jansen, A. N. An All-Organic Non-aqueous Lithium-Ion Redox Flow Battery. *Adv. Energy Mater.* **2012**, *2*, 1390−1396.
(58) Compton, R. G.; Banks, C. E. *Understanding Voltammetry*, 2nd ed.; Imperial College Press: London, 2011.
(59) Goulet, M.-A.; Aziz, M. J. Flow Battery Molecular Reactant Stability Determined by Symmetric Cell Cycling Methods. *J. Electrochem. Soc.* **2018**, *165*, A1466−A1477.
(60) Bard, A. J.; Faulkner, L. R. *Electrochemical Methods: Fundamentals and Applications*, 6th ed.; Wiley: New York, 2001.

DOI: 10.1021/acs.chemmater.8b04770
Chem. Mater. 2019, 31, 4353−4363

(61) Laramie, S. M.; Milshtein, J. D.; Breault, T. M.; Brushett, F. R.; Thompson, L. T. Performance and Cost Characteristics of Multi-Electron Transfer, Common ion Exchange Non-aqueous Redox Flow Batteries. *J. Power Sources* **2016**, *327*, 681−692.
(62) Milshtein, J. D. Electrochemical Engineering of Low-Cost and High-Power Redox Flow Batteries. Ph.D. Dissertation, Massachusetts Institute of Technology, Cambridge, MA, 2017.

DOI: 10.1021/acs.chemmater.8b04770
Chem. Mater. 2019, 31, 4353−4363